Applied Catalysis B: Environmental 259 (2019) 118042

Contents lists available at ScienceDirect

Applied Catalysis B: Environmental

journal homepage: www.elsevier.com/locate/apcatb

Atomically dispersed Fe-N-C derived from dual metal-organic frameworks as efficient oxygen reduction electrocatalysts in direct methanol fuel cells

Xinlong Xu[a,b], Zhangxun Xia[a], Xiaoming Zhang[a], Ruili Sun[a,b], Xuejing Sun[a,b], Huanqiao Li[a], Chuchu Wu[a,b], Junhu Wang[a], Suli Wang[a,*], Gongquan Sun[a,*]

[a] Division of Fuel Cell & Battery, Dalian National Laboratory for Clean Energy, Dalian Institute of Chemical Physics, Chinese Academy of Sciences, Dalian 116023, China
[b] University of Chinese Academy of Sciences, Beijing 100049, China

ARTICLE INFO

Keywords:
Direct methanol fuel cells
Electrocatalysts
Metal-organic frameworks
Oxygen reduction reaction
Atomically dispersed Fe atoms

ABSTRACT

The rational design of highly efficient, low-cost and methanol-tolerant catalysts toward the oxygen reduction reaction (ORR) is urgently desired for the commercialization of direct methanol fuel cells (DMFCs). Herein, a novel Fe-N-C catalyst (ZIF/MIL-10-900) is derived from a mixture of ZIF-8 and MIL-101(Fe) and atomically dispersed FeN_4 structures are confirmed by Mössbauer spectra and X-ray absorption spectroscopy. Study on the pyrolysis procedure reveals that Fe atoms in FeN_4 are from MIL-101(Fe), while ZIF-8 acts as structural support and nitrogen sources. The as-prepared catalyst demonstrates a comparable ORR activity with the commercial Pt/C possessing a half-wave potential ($E_{1/2}$) of 0.78 V in acids, in combination with excellent methanol tolerance and stability. One of the highest peak power density of 83 mW cm^{-2} in DMFC (3 M CH_3OH) by adopting ZIF/MIL-10-900 as cathode catalyst is obtained, which is 2.8-fold higher than that of the commercial Pt/C in the same operating condition.

1. Introduction

Polymer electrolyte membrane fuel cells (PEMFCs) have been considered as promising solutions to meet the future energy requirements due to highly efficient energy conversion and environmentally friendly features. [1–3] Among PEMFCs, DMFCs have gained intensive attraction for the use of liquid fuel, which is convenient for storage and transportation [4–7]. However, the commercialization of DMFCs is hampered by the expensive and scarce platinum-based catalysts, especially for the sluggish ORR in the cathode [8,9]. Furthermore, their performance is severely limited by methanol crossover, which leads to catalyst poisoning and a mixed potential [10]. Therefore, extensive investigations have been devoted to explore low-cost and methanol-tolerant catalysts for ORR [11–15]. In particular, Fe-N-C catalysts are expected to replace expensive Pt-based catalysts owing to their intrinsic nature of methanol tolerance and considerable ORR activity in acid medium [6,16–18]. Experiments combined with density functional theory (DFT) calculations reveal the excellent ORR activity could be generated from Fe-N_x species formed by coordination of Fe with nitrogen. [19–21] Hence, atomically dispersed Fe-N-C catalysts with homogenous Fe-N_x active sites have been intensively studied in pursuit of the maximum metal utilization and high electrocatalytic performance. [22–24] In recent works, H_2-O_2 PEMFCs using atomically dispersed Fe-N-C catalysts exhibit excellent performance with a highest power density over 1 W cm^{-2} [25,26]. These works demonstrate the possibility of the application of atomically dispersed Fe-N-C catalysts in DMFCs on account of the same ORR process in the cathodes. Thus the application of atomically dispersed Fe-N-C catalysts in DMFCs is highly expected, but has not been reported yet.

In recent years, metal-organic frameworks (MOFs) have emerged as promising precursors for synthesizing Fe-N-C materials. [19,20,23,25,27–37] ZIF-8 is one of the most popular nitrogen-carbon precursors for its extremely high specific surface area and abundant nitrogen content [23,25,33,35,36]. Fe based MIL is widely chosen as the Fe precursor for abundant and homogenously dispersed Fe atoms [27–30,34]. However, it is worth noting that MIL generally removes the oxygen-containing functional groups attached to the metal during carbonization [38], resulting in the collapsion of the morphology as well as the porous structure. The low specific surface area of derived carbon is insufficient for the distribution of Fe, thus forming inactive Fe nanoparticles and Fe carbide. Therefore, high specific surface area supports or support precursors are commonly introduced during synthesizing Fe-N-C from MIL. Additional nitrogen sources are also required because of the absence of nitrogen in most MILs [27,29,30,39,40]. Recent progress

* Corresponding authors.
E-mail addresses: suliwang@dicp.ac.cn (S. Wang), gqsun@dicp.ac.cn (G. Sun).

https://doi.org/10.1016/j.apcatb.2019.118042
Received 5 May 2019; Received in revised form 23 July 2019; Accepted 1 August 2019
Available online 10 August 2019

suggests that combining different kinds of MOFs can take their respective advantages, which inspires us to obtain efficient Fe-N-C catalysts from high surface area and nitrogen-rich ZIF-8 and Fe-containing MIL [31,32].

Herein, a dual-MOFs strategy is developed to prepare atomically dispersed Fe-N-C catalyst (ZIF/MIL-10-900) for ORR in DMFCs. The precursor (ZIF/MIL-10) is prepared by mechanically grinding ZIF-8 together with MIL-101(Fe), and the advantages such as convenience and environmental amity of such solid methods have already been highlighted by many researchers. [18,25] Control experiments showed that the combination of ZIF-8 and MIL-101(Fe) not only provides sufficient surface area for finely atomic dispersion, but also prevents Fe agglomeration during pyrolysis. The majority of Fe atoms in ZIF/MIL-10-900 exhibit FeN_4 configuration as reveled by Mössbauer spectrum and X-ray absorption spectroscopy (XAS). Remarkable ORR activity and DMFC performance of ZIF/MIL-10-900 was demonstrated with enhanced durability. These results demonstrate the promising prospect for high performance and inexpensive DMFCs by using non-precious metal catalysts.

2. Experimental section

All the reagents and solvents were commercially available and directly used without any purification.

2.1. Synthesis of ZIF-8 and MIL-101(Fe)

ZIF-8 was synthesized using the reported recipe with modifications. [41] 6.52 g 2-methylimidazole and 3.26 g $Zn(NO_3)_2.6H_2O$ were dissolved in 200 mL methanol, respectively. Then the salt solution was subsequently injected into the ligand solution under vigorously stirring for 1 h at room temperature. The suspension was seperated by centrifugation. The final product was collected after washing three times with methanol and drying overnight in an 80 °C vacuum oven.

MIL-101(Fe) was prepared according to the literature with slightly modifications. [42] 0.535 g $FeCl_3.6H_2O$, 0.329 g terephthalic acid (TPA) and 1.8 ml acetic acid were mixed in a solvent of 56 ml *N,N-d*imethylformamide (DMF). The precursor solution was transferred to an autoclave and reacted at 120 °C for 24 h. The synthesized MIL-101(Fe) solid was collected and washed with DMF and methanol thoroughly by centrifugation, then dried in an 80 °C vacuum oven overnight.

2.2. Synthesis of ZIF/MIL-x-900 and ZIF/$FeCl_3$-900

The catalyst precursors ZIF/MIL-x (x denoted as the mass ratio of ZIF-8 and MIL-101(Fe)) were prepared by grinding 500 mg ZIF-8 and MIL-101(Fe) with different mass ratio (100:1, 20:1, 10:1, 5:1) to form a uniform light yellow powder. Then the precusors were pyrolyzed at 900 °C for 2 h under a N_2 flow of 100 mL min^{-1} and a heating rate of 5 °C min^{-1}. The pyrolysis products were leached with 200 mL of 1 M HCl solution at room temperature for 12 h. Finally, the ZIF/MIL-x-900 were washed with 2 L deionized water by filtration and dried for 8 h in an 80 °C vacuum oven.

ZIF/$FeCl_3$-900 catalyst had the same preparing procedure with ZIF/MIL-x-900 but MIL-101(Fe) was replaced to 54 mg $FeCl_3.6H_2O$ and 33.5 mg TPA to make sure the precursors of ZIF/MIL-10-900 and ZIF/$FeCl_3$-900 had the same elemental composition but different structures.

2.3. Physical characterization

JEOL JEM-ARM200 F STEM/TEM was used to collect images at atomic resolution. X-ray absorption spectra (XAS) were collected at the BL 14W1 of Shanghai Synchrotron Radiation Facility, Shanghai Institute of Applied Physics, China. Scanning electron microscopy(SEM) and transmission electron microscopy (TEM) characterization were carried out with JSM-7800 F and JEM-2100 F from JEOL, respectively. X-ray diffraction (XRD) was performed using a Rigaku D/Max-2500 diffractometer. X-ray photoelectron spectroscopy (XPS) analysis were carried out with an Al Kα X-ray source (Thermo Fisher). N_2 adsorption isotherms were performed at 77.4 K using a Quantachrome NOVA 2200e instrument. Thermogravimetric analysis (TGA) curves were tested on SDT Q600 (TA instruments) with a heat rate of 10 °C min^{-1} under Ar. The metal loadings of the catalysts were determined with ICP-OES on an IRIS Intrepid II XSP instrument (Thermo Electron Corp.). Energy dispersive X-ray fluorescence spectrum (EDXRF) was performed on an Thermo Fisher ARL QUANT'X instrument.

2.4. Electrochemical measurements

Electrochemical measurements were conducted on a CHI 760D electrochemical station using a saturated calomel electrode(SCE) and a platinum sheet as the reference and counter electrodes. The catalyst ink was obtained by ultrasonically dispersing 4 mg of Fe-N-C or Pt/C (20 wt % Pt on Vulcan XC-72, Hispec3000, Johnson Matthey Fuel Cells Ltd) catalysts in 2 mL ethanol contained 0.05 wt% Nafion®. The glass carbon rotating disk electrode (RDE, d = 5.00 mm) and rotating ring disk electrode (RRDE, d = 5.61 mm) were polished with alumina slurry and cleaned with DI water repeatedly, then dried under room temperature. The ink was droped on the glass carbon and dried under ambient condition to give loadings of 0.5 mg cm^{-2} for Fe-N-C or 0.1 mg cm^{-2} for Pt/C, respectively. The LSV curves for ORR were obtained in O_2-saturated 0.1 M $HClO_4$ by deducting the background tested in N_2-saturated electrolyte to avoid the effect of double layer capacitance.

The Koutecky − Levich (K − L) plots were obtained at various rotating speeds. The kinetic current densities (j_k) and the electron transfer number (n) were calculated from the K-L equations:

$$\frac{1}{j} = \frac{1}{j_k} + \frac{1}{j_l} = \frac{1}{j_k} + \frac{1}{B\omega^{1/2}}$$

$$B = 0.62nFC_O D^{2/3} v^{-1/6}$$

The electron transfer number (n) and H_2O_2 yield based on the RRDE results were calculated from the following equations:

$$H_2O_2(\%) = \frac{2\frac{I_R}{N}}{\frac{I_R}{N} + I_D} * 100\%$$

$$n = 4 * \frac{I_D}{\frac{I_R}{N} + I_D}$$

Here, I_D and I_R were the disk and ring currents, respectively, and N was the ring collection efficiency (0.37).

2.5. DMFC single-cell test

The catalyst ink containing 22 mg Fe-N-C catalyst and 440 mg 5 wt % Nafion® ethanol solution was ultrasonically dispersed for 1 h and coated on a 2*2 cm^{-2} PTFE-pretreated carbon paper (Toray 060) with microporous layer. The catalyst loading of as-prepared Fe-N-C cathode was 4.0 mg cm^{-2} and the ionomer content was 50 wt%. The anode was prepared by coating PtRu black catalyst (Johnson Matthey Fuel Cells Ltd., 6 mg $cm^{-2)}$ and Nafion®ionomer (15 wt%) on the carbon paper to form a gas diffusion electrode (GDE). Then the membrane electrode assembly (MEA) was prepared by hot-pressing cathode, anode, Nafion® 212 membrane at about 1.5 MPa for 5 min at 130 °C.

Fuel cell tests were conducted at a homemade DMFC test system with an Arbin loading at 80 °C. The flow rates of methanol with different concentration were 1.0 mL min^{-1}. The O_2/air flow rates were 80 sccm without back-pressure and humidification.

3. Results and discussion

3.1. Morphological and structural characterizations

ZIF-8 and MIL-101(Fe) were firstly synthesized and confirmed by SEM observation (Figure S1) and XRD patterns (Figure S2). Then the as-prepared ZIF-8 (act as support precursor) and MIL-101(Fe) (act as Fe precursor) were mixed mechanically with different mass ratios of 100:1, 20:1, 10:1 and 5:1 to obtain ZIF/MIL-x, where x denoted as the mass ratio. In order to emphasize the advantages of the dual MOF strategy, a control sample denoted as ZIF/$FeCl_3$ was prepared by mixing ZIF-8 together with $FeCl_3.H_2O$ (a general Fe precursor chosen for preparing Fe-N-C [43–46]) and TPA. It should be noticed that the Fe contents in ZIF/MIL-10 and ZIF/$FeCl_3$ are consistent for the convenience of comparison according to XRF results (Figure S3). One-step pyrolysis at 900 °C and subsequent acid-leaching were performed to obtain Fe-N-C catalysts denoted as ZIF/MIL-x-900 and ZIF/$FeCl_3$-900, respectively.

Due to the poor thermostability of inorganic Fe salts, agglomerated FeNPs are clearly observed in the SEM image of ZIF/$FeCl_3$-900 (Figure S4a) especially under the backscattering electron mode (Figure S4b) with more sensitive contrast. And the TEM images (Fig. 1a and Figure S5) demonstrate that those FeNPs are well encapsulated with carbon layer thus cannot be removed by acid-washing. Surprisingly, no evident crystalline nanoparticles are observed in ZIF/MIL-10-900 (Fig. 1b, c) though EDS (Figure S6) and ICP-OES verifies the existing of Fe (2.1 wt %), indicating that the Fe species must be dispersed at a smaller scale that is invisible under ordinary SEM and TEM. Aberration-corrected scanning transmission electron microscopy (AC-STEM) further reveals a number of bright spots at atomic scale under high-angle annular dark field (HAADF) mode, corresponding to abundant Fe with atomic dispersion in ZIF/MIL-10-900 (Fig. 1d). The EDS mapping images (Fig. 1e) also disclose the homogeneous distribution of Fe and N elements are on the carbon matrix.

XRD patterns (Fig. 2a) further confirm that peaks of Fe carbide are absent in the samples of ZIF/MIL-10-900, ZIF/MIL-20-900 and ZIF/MIL-100-900, but observed in ZIF/MIL-5-900 and ZIF/$FeCl_3$-900. The sharper (002) graphite carbon peaks of ZIF/MIL-5-900 and ZIF/$FeCl_3$-900 also suggest the catalytic graphitization by metallic Fe. Mössbauer spectroscopy is extremely effective to analyze the electronic structure and coordination environment of various Fe moieties. The Mössbauer spectra of ZIF/MIL-10-900 and ZIF/$FeCl_3$-900 are illustrated in Fig. 2b, c and Table 1 lists the fitting parameters and the proportion of different Fe species calculated from the relative areas. The spectrum of ZIF/MIL-10-900 can be well-fitted with three components: two doublets denoted as D1 and D2 are assigned to FeN_4 at low and medium spin states, respectively. A sextet (Sext1) corresponding to Fe carbide is also detected with a minimal amount of only 8.25%, thus undetectable in XRD. By contrast, one singlet and four sextets corresponding to γ-Fe (S1), α-Fe (Sext1) and Fe_5C_2 (Sext2-4, three types of Fe in the unit cell) appear in the spectrum of ZIF/$FeCl_3$-900 beside a doublet (D1). [47–51] The dominant content of crystalline Fe is 77.68% yet the Fe-Nx species (D1) is only 22.32%. The FeN_4 structure in ZIF/MIL-10-900 is ulteriorly determined by X-ray absorption near-edge structure (XANES) and extended X-ray absorption fine structure (EXAFS). The XANES spectrum (Fig. 2d) of Fe K-edge shows the similarity of ZIF/MIL-10-900 and Fe(II) phthalocyanine (Fe(II)Pc). In the EXAFS spectrum (Fig. 2e), a significant peak observed at ~1.5 Å for ZIF/MIL-10-900 is generally

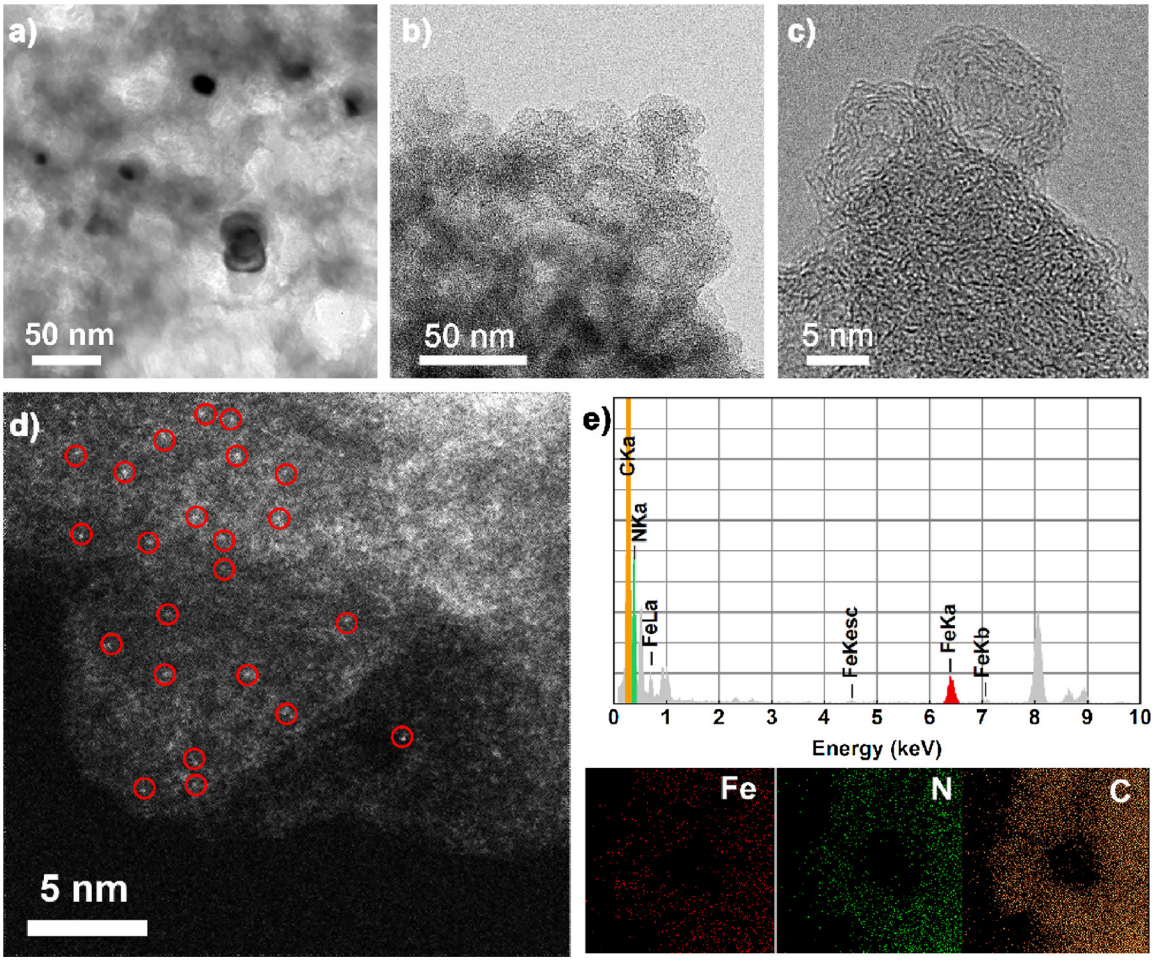

Fig. 1. (a) TEM image of ZIF/$FeCl_3$-900. (b) TEM, (c) HRTEM, (d) HADDF-STEM images and (e) elemental mapping of ZIF/MIL-10-900.

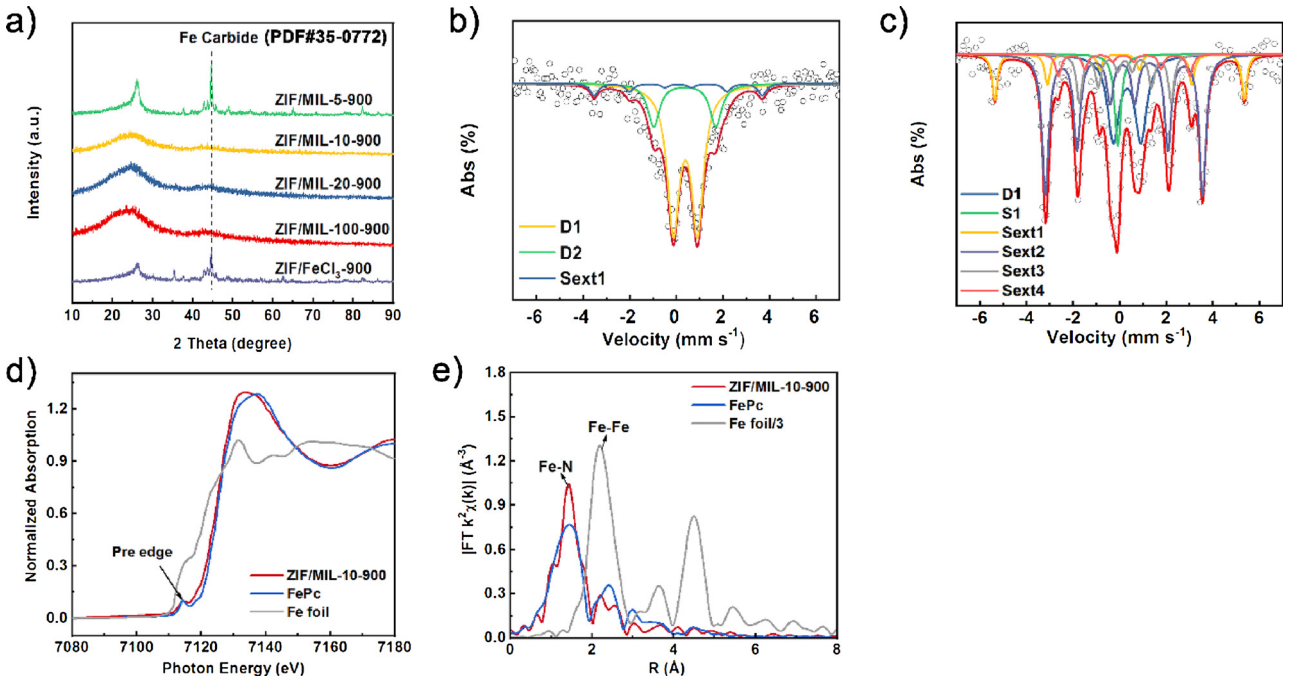

Fig. 2. (a) XRD patterns of ZIF/MIL-x-900 and ZIF/$FeCl_3$-900. Mössbauer spectra of (b) ZIF/MIL-10-900 and (c) ZIF/$FeCl_3$-900. (d) Normalized XANES spectra at Fe K-edge and (e) Fourier-transformed EXAFS spectra of ZIF/MIL-10-900, FePc and Fe foil.

Table 1
The fitted Mössbauer parameters and the corresponding assignment to ZIF/MIL-10-900 and ZIF/$FeCl_3$-900.

Sample	Fe species	IS/ mm s^{-1}	QS/ mm s^{-1}	Area %	assignment
ZIF/MIL-10-900	D1	0.39	1.03	70.92	Fe(II)N_4 low spin
	D2	0.36	2.67	20.83	Fe(II)N_4 medium spin
	Sext1	0.08	–	8.25	Fe carbide
ZIF/$FeCl_3$-900	D1	0.32	1.18	22.32	Fe(II)N_4 low spin
	S1	−0.07	–	6.49	γ-Fe
	Sext1	0	–	10.7	α-Fe
	Sext2	0.16	0.06	42.74	Fe_5C_2
	Sext3	0.24	0.01	12.06	
	Sext4	0.17	0.04	5.63	

considered as Fe-N bonds. [19,20,25,49,52] This result is in accordance with the HAADF-STEM and Mössbauer spectra analysis that the majority of Fe atoms in ZIF/MIL-10-900 exhibit atomically dispersed FeN_4 configuration. According to literatures [47,50], D1 sites with Fe in low spin state possess exceptional ORR activity, attributing to the empty $3dz^2$ orbit that facilitates the end-on adsorption of oxygen, which is indicative for an outstanding ORR performance of ZIF/MIL-10-900. But the crystalline α-Fe, β-Fe and Fe_5C_2 in the ZIF/$FeCl_3$-900 are commonly considered inactive to ORR.

3.2. Study on the formation process

It is well known that the separate pyrolysis of ZIF-8 and MIL-101(Fe) will form N-doped carbon and Fe carbide/C, respectively. Therefore, the reason for the formation of atomically dispersed FeN_4 in the ZIF/MIL-10-900 has to be further investigated. According to recent reports, the morphology of Fe-N-C prepared from MILs are amorphous or consistent with the additional carbon support [29,30,34,39], which is obviously different from ZIFs and UiOs (a class of MOFs firstly developed by researchers from University of Oslo) [23,35,53]. In our work, we also observe that the octahedral morphology of MIL-101(Fe) collapses into amorphous fragments after pyrolysis in the SEM image (Figure S7) and large amounts of Fe carbide produces as shown in the XRD results (Figure S8). According to the N_2 adsorption-desorption isotherm measurements (Figure S9 and Table S1), the Brunauer-Emmett-Teller (BET) specific surface area of MIL-101(Fe) is only 415 $m^2 g^{-1}$ and reduced to 202 $m^2 g^{-1}$ after heat treatment. But the specific surface areas of ZIF/MIL-x-900 increase gradually as the increased ratio "x" of ZIF-8 in the precursors and the shape of isotherms and calculated pore distribution get similar to that of pyrolyzed-ZIF-8 (Fig. 3a and Figure S10-11). Meanwhile, the signals of crystalline Fe in the XRD disappear (Fig. 2a), indicating the high specific surface area of ZIF-8 serves the dispersion of Fe. Moreover, MIL-101(Fe) decomposes earlier than ZIF-8 during heating-up, but is not fully carbonized when ZIF-8 begins to lose weight according to the TG analysis (Fig. 3b), which prevents MIL-101(Fe) from being fully converted to Fe carbide/C before the formation of support. In particular, the pyrolysis of ZIF-8 and MIL-101(Fe) is coupled at the range of 600–700 °C. XPS at different temperatures (Figure S12 and Table S2) is conducted and proves that 600–700 °C is the critical range for formation FeN_4 sites. The N1 s high-resolution XPS spectrums (Fig. 3c and Table 2) reveal that the majority of N at 600 °C still coincides with the C = N symmetry peak, similar to that of the initial ZIF-8 but with a small amount of pyridinic N formed. [23] But N1 s shifts to higher energy and the Fe-N peak (˜399.7 eV) appears when the temperature rising to 700 °C and the amount of Fe-N keeps increasing until 900 °C [54–58]. In contrast, we observe that $FeCl_3.6H_2O$ completely aggregates into Fe_2O_3 before 500 °C and the corresponding weight loss can be also observed in the curve of ZIF/$FeCl_3$ (Figure S13). The XPS analysis (Figure S14) of ZIF/$FeCl_3$-900 has also been conducted and we can observe that it has lower Fe-N content but higher graphitic N content than ZIF/MIL-10-900 in the N1 s spectra. That's because numerous Fe nanoparticles instead of FeNx species form in the ZIF/$FeCl_3$-900 and the Fe nanoparticles can further catalyze graphitization, which is consistent with the structural characterizations discussed in Section 3.1.

We assume the formation process of ZIF/MIL-10-900 according these results discussed above as illustrated in Fig. 4a. Firstly, MIL-101(Fe) disintegrates and collapses into fragments, making good

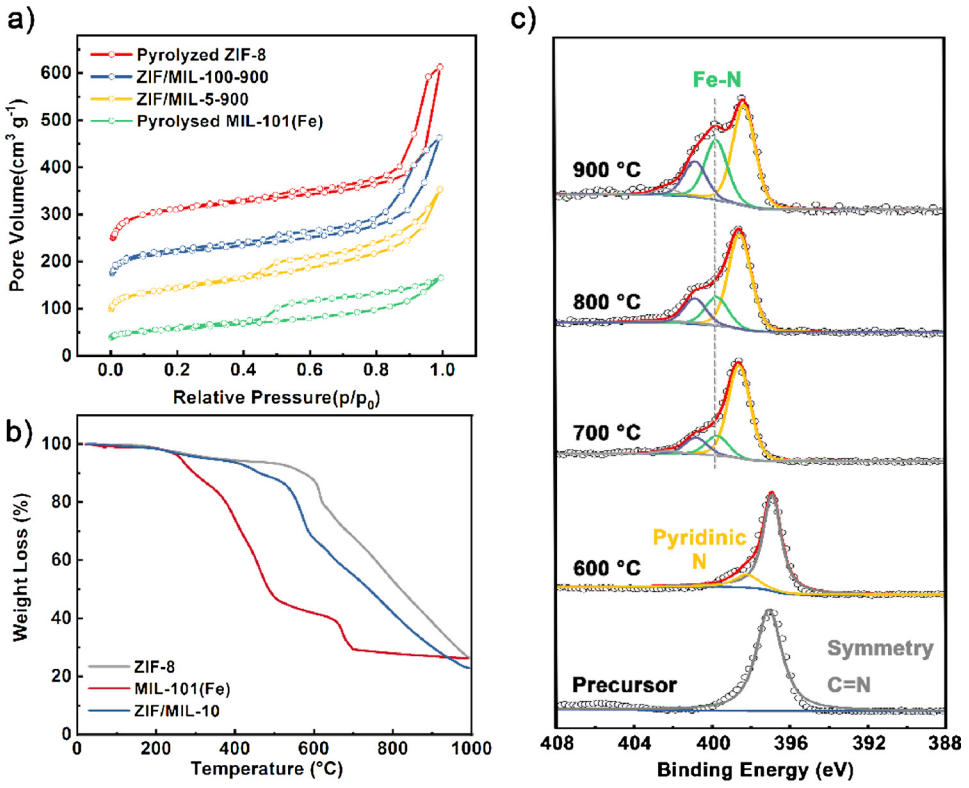

Fig. 3. (a) Nitrogen sorption isotherms of pyrolyzed ZIF-8, ZIF/MIL-100-900, ZIF/MIL-5-900, and pyrolyzed MIL-101(Fe). (b) TGA curves of ZIF-8, MIL-101(Fe) and ZIF/MIL-10 under an Ar flow of 100 mL min^{-1}. (c) High resolution N 1s spectra of ZIF/MIL-10 pyrolyzed at different temperature.

Table 2
Summary of the content of different N species in the N1 s high resolution spectra of ZIF/MIL-10 pyrolyzed at different temperatures.

	C = N 397.6 eV	Pyridinic N 398.5 eV	Fe-N 399.7 eV	Pyrrolic N 400.8 eV	Graphitic N 402.2 eV
ZIF/MIL	100%	–	–	–	–
600 °C	84.68%	15.32%	–	–	–
700 °C	–	70.21%	14.92%	12.69%	2.18%
800 °C	–	61.94%	18.79%	16.41%	2.86%
900 °C	–	49.59%	29.56%	17.52%	3.33%

contact with the out surface of the unreacted ZIF-8 from 300 to 600 °C. Subsequently, ZIF-8 begins to carbonize into support while Fe in the MIL-101(Fe) fragments is coordinated with N in ZIF-8 to form FeNx sites. Meanwhile, part of the Fe that is not contacted to ZIF-8 transform into Fe carbide. After acid leaching, only a minimal amount of Fe carbide remain which is observed under the ultra-sensitive Mössbauer spectrum but invisible under XRD.

According to our hypothesis, the final morphology of the ZIF/MIL-10-900 sample should be similar to the dodecahedron of ZIF-8 because of the collapse of MIL-101(Fe). However, ZIF-8 with a diameter of only 30 nm was selected during preparation of catalysts in order to obtain better performance according to the previous literature. [23,59] As a result, the morphology after pyrolysis is difficult to be distinguished. Therefore, we further synthesized ZIF/MIL-10-900 using ZIF-8 with larger sizes of 60,120 and 400 nm. All the catalysts exhibit dodecahedral polyhedron of ZIF-8 with different sizes under SEM and TEM (Fig. 4b-g), while no MIL-101(Fe) structure was observed. Moreover, XRD patterns of ZIF/MIL-10-900 prepared from ZIF-8 with different sizes present none peaks of Fe carbide, thus proving our assumption (Figure S15).

3.3. Electrochemical catalytic performance

The ORR activities of as-prepared Fe-N-C and the commercial Pt/C catalyst were investigated in 0.1 M $HClO_4$ solution by cyclic voltammetry (CV) and linear sweep voltammetry (LSV). It is found in LSV polarization curves (Fig. 5a) that ZIF/$FeCl_3$-900 generates poor ORR activity with a half-wave potential ($E_{1/2}$) of 0.65 V (vs. RHE) and the limited current density (j_l, current density at 0.5 V) of 3.9 mA cm^{-2}. However, ZIF/MIL-10-900 exhibits a much higher j_l of 5.9 mA cm^{-2} and more positive $E_{1/2}$ of 0.78 V (vs. RHE). Tafel plots (Fig. 5b) also demonstrate that ZIF/MIL-10-900 delivers a slope of 59.2 mV dec^{-1} which is similar to that of Pt/C (62.1 mV dec^{-1}) but far smaller than ZIF/$FeCl_3$-900 (83.5 mV dec^{-1}), indicating higher intrinsic activity of FeN_4 sites than crystalline Fe species. The electrochemical performance of pyrolyzed-ZIF-8 and pyrolyzed-MIL-101(Fe) are also provided in Figure S16 and both of them exhibit poor performance because N-doped C and Fe carbide/C are commonly considered inactive for ORR in acids. For the catalysts prepared by the dual-MOFs strategy, a volcano-like trend of the ORR activity is observed with the $E_{1/2}$ shifting from 0.74 V for ZIF/MIL-100-900 to 0.78 V for ZIF/MIL-10-900 and back to 0.72 V for ZIF/MIL-5-900. This is because the density of Fe-N_x active sites could be increased with the rising amount of MIL-101(Fe) until inactive Fe agglomeration forms in ZIF/MIL-5-900 with MIL-101(Fe) overmuch. CV curves (Figure S17), consisting of double layer capacitance and the pseudocapacitance [60], also reveal the sharp decrease in the electrochemical surface area of ZIF/MIL-5-900, in line with its relatively low BET specific surface area.

RRDE tests (Fig. 5c, d) demonstrate that ORR on ZIF/MIL-10-900 follows a near-4 electron pathway between 0.2 and 0.8 V (vs. RHE) and yields H_2O_2 less than 5%, which is in accordance with the result calculated from K-L plots (Figure S18). Significantly, the ZIF/MIL-10-900 catalyst shows a much better methanol tolerance than the commercial Pt/C (Fig. 5e and Figure S19), which makes it a promising candidate operating in the cathode of DMFCs. The durability of ZIF/MIL-10-900

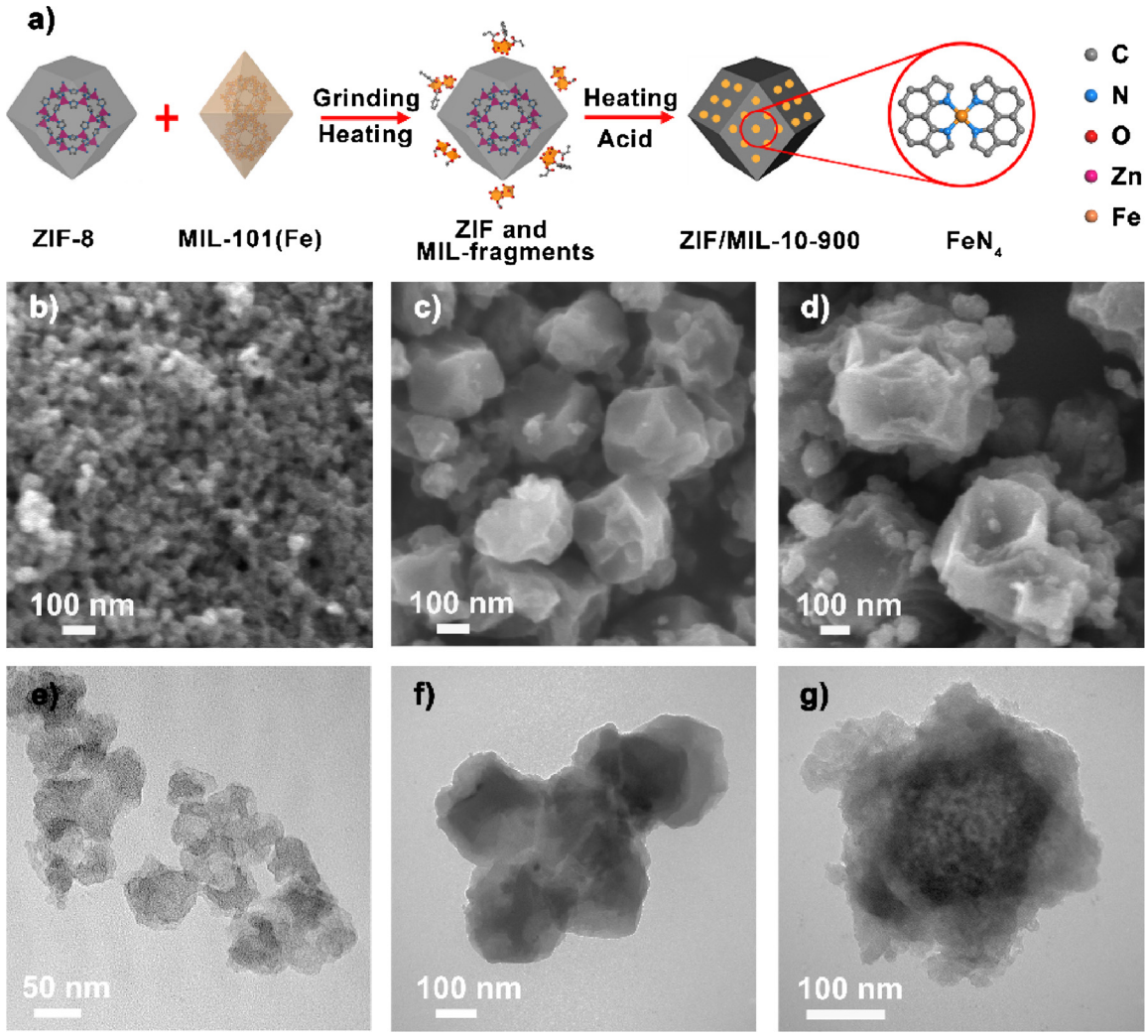

Fig. 4. (a) The inferred synthetic process of the dual-MOFs strategy. SEM (b, c, d) and TEM (e, f, g) images of ZIF/MIL-10-900 synthesized from ZIF-8 with size of 60 nm, 120 nm and 400 nm.

was evaluated by the chronoamperometry at a constant potential of 0.5 V and 0.7 V (Fig. 5f and Figure S20). Fig. 5f shows a 95.9% current retention for the ZIF/MIL-10-900 after 40000 s at 0.5 V (vs. RHE), higher than 69.7% of Pt/C. Furthermore, a poisoning experiment was performed utilizing SCN^- (Figure S21). A significant performance decay is observed because the strongly adsorbed SCN^- limits the access of O_2 to Fe, which confirms the high ORR activity of ZIF/MIL-10-900 could be attributed to FeN_4 sites. [61]

ZIF/MIL-10-900 (4 mg cm^{-2}) was assembled as the cathode catalyst layer of a 4 cm^2 DMFC to investigate the single cell performance operated on O_2 without humidification and back pressure. The performances of DMFCs fabricated with ZIF/$FeCl_3$-900 and Pt/C (0.5 mg_{Pt} cm^{-2}) were also investigated for comparison. At a low-concentration methanol of 0.5 M in the anode, the peak power density (P_{max}) of ZIF/MIL-10-900 is 64 mW cm^{-2}, significantly superior to that of ZIF/$FeCl_3$-900 (28 mW cm^{-2}) but inferior to that of Pt/C (85 mW cm^{-2}) (Fig. 6a), owing to the higher activity of Pt/C and faster mass transfer due to the thinner catalyst layer [24]. Anode fed with higher concentration methanol in DMFCs will improve the electrochemical reaction as well as reduce the fuel weight and volume. However, a poor open-circuit voltage (0.475 V) and P_{max} (31.8 mW cm^{-2}) is observed in Pt/C equipped DMFC fed with 3 M methanol solution, because methanol crossover scales up significantly. Conversely, the open-circuit voltage of DMFC with ZIF/MIL-10-900 cathode is changeless under 3 M methanol benefitting from its superior methanol tolerance. Moreover, a performance enhancement is observed because of faster kinetics under higher reactant concentration in the anode. As a result, the P_{max} of ZIF/MIL-10-900 sample reaches up to 83 mW cm^{-2}, which is 2.8-fold greater than that of Pt/C (Fig. 6b). When the methanol concentration increases to 5 M, excellent cell performance of ZIF/MIL-10-900 is still available, whereas the Pt/C cathode can hardly work (P_{max} = 25.8 mW cm^{-2}) (Figure S22). The DMFC performance of ZIF/MIL-10-900 operated on air is also tested and the P_{max} is 30.3 mW cm^{-2} with 0.5 M methanol fed in the anode (Figure S23). The unsatisfactory performance can be attribute to the higher mass-transport resistance in the cathode. [24] Furthermore, the short durability tests are performed at a constant current density of 100 mA cm^{-2} (Fig. 6c) and at a constant voltage of 0.4 V (Figure S24). In Fig. 6c, the DMFC equipped with ZIF/MIL-10-900 exhibits good durability with only 29% voltage loss after a 24 h test. Both the performance and durability of this dual-MOFs derived ORR catalyst are among the top level of NPMCs measured in DMFCs reported previously (Table S3). These results make the dual-MOFs strategy an ideal approach to prepare cathode catalysts in DMFCs, and other devices with O_2 cathodes.

4. Conclusion

In summary, a dual-MOFs strategy has been established to develop atomically dispersed Fe-N-C as cathode catalyst in DMFCs. The investigation on the formation process reveals that ZIF-8-derived support

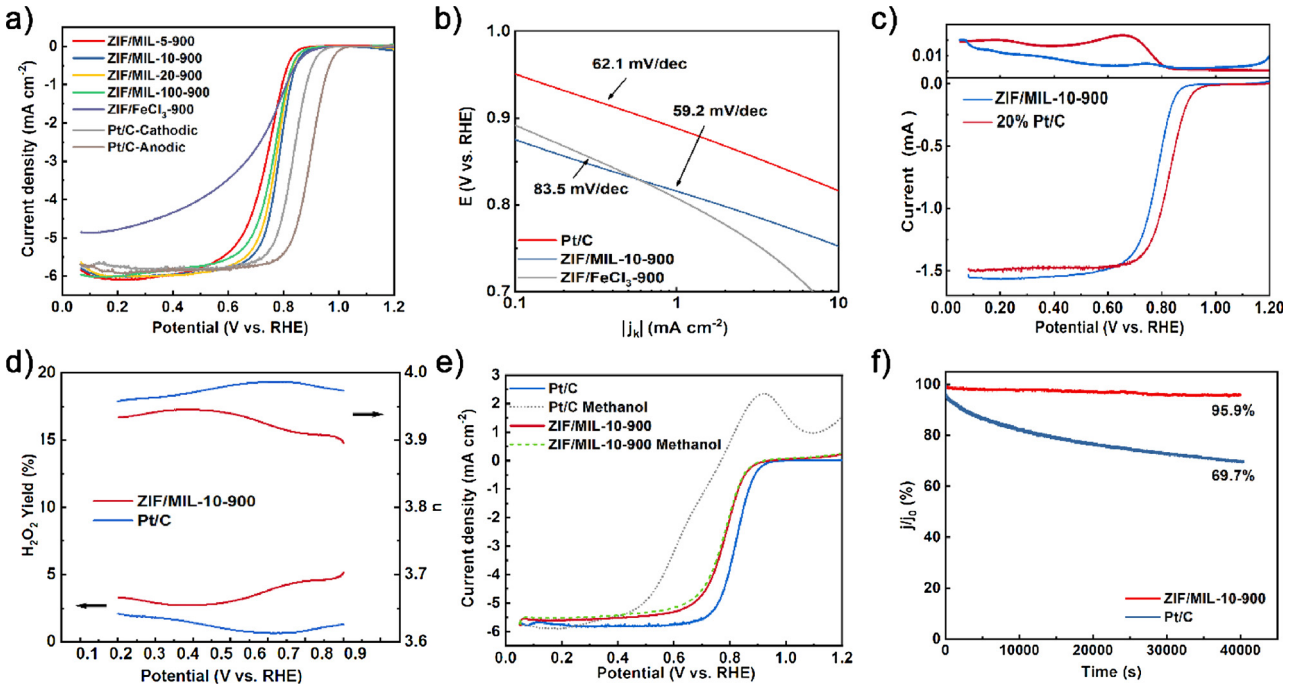

Fig. 5. (a) LSV curves of ZIF/MIL-x-900, ZIF/$FeCl_3$-900 and Pt/C determined by RDE tests in O_2-saturated 0.1 M $HClO_4$ at a scan rate of 10 mV s^{-1} and a rotating speed of 1600 rpm. (b) Tafel plots of ZIF/MIL-10-900, ZIF/$FeCl_3$-900 and Pt/C and the plots of Pt/C were calculated from the cathodic sweep result. (c) LSV curves of ZIF/MIL-10-900 and Pt/C recorded by RRDE at the same condition as RDE tests and the potential of Pt ring was constant at 1.2 V. (d) Electron transfer number and H_2O_2 yield of ZIF/MIL-10-900 and Pt/C calculated from the RRDE results. (e) Methanol-tolerance measurement from the LSV curves of ZIF/MIL-10-900 and Pt/C with or without 0.1 M methanol. (f) The chronoamperometric test of ZIF/MIL-10-900 and Pt/C at 0.5 V.

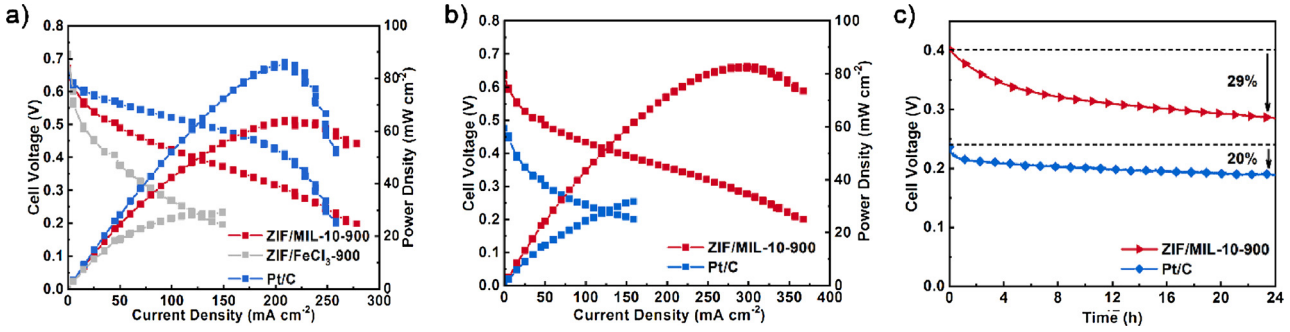

Fig. 6. I–V polarization and power density curves of ZIF/MIL-10-900, ZIF/$FeCl_3$-900 and Pt/C with different concentration of methanol: (a) 0.5 M CH_3OH, (b) 3 M CH_3OH. (c) Short term durability test of ZIF/MIL-10-900 and Pt/C in DMFC with 3 M CH_3OH. Anode: 6 mg cm^{-2} PtRu black, 1 mL min^{-1} CH_3OH with different concentration; Cathode: 4 mg cm^{-2} for Fe-N-C catalysts or 0.5 mg_{Pt} cm^{-2} for Pt/C, 80 sccm O_2; Temperature: 80 °C.

provides abundant specific surface area and nitrogen while the collapsing MIL-101(Fe) provides Fe to form the atomically dispersed active sites. ZIF/MIL-10-900 with abundant FeN_4 sites exhibits comparable ORR activity, better stability and superior methanol tolerance compared with the commercial Pt/C. DMFC equipped with ZIF/MIL-10-900 delivers a P_{max} of 83 mW cm^{-2} at 3 M methanol fueled with enhanced durability, making it a promising substitute for precious metal ORR catalysts. The current study highlights the advantages and prospect of atomically dispersed Fe-N-C catalysts in the application of DMFCs, and also enables this new fabrication strategy a promising approach towards advanced catalytic materials for energy conversion devices.

Declaration of Competing Interest

The authors declare that they have no known competing financial interests or personal relationships that could have appeared to influence the work reported in this paper.

Acknowledgements

This work was financially supported by the Key Program of the Chinese Academy of Sciences (KFZD-SW-419), National Natural Science Foundation of China (21503228). We also acknowledge the staff of the BL14W1 beamline at the Shanghai Synchrotron Radiation Facility for assistance with the X-ray absorption spectroscopy measurements. We thank Prof. Alexandre Rykov for Mössbauer spectra discussions particularly.

Appendix A. Supplementary data

Supplementary material related to this article can be found, in the online version, at doi:https://doi.org/10.1016/j.apcatb.2019.118042.

References

[1] M. Shao, Q. Chang, J.P. Dodelet, R. Chenitz, Recent advances in electrocatalysts for oxygen reduction reaction, Chem. Rev. 116 (2016) 3594–3657.

[2] F.T. Wagner, B. Lakshmanan, M.F. Mathias, Electrochemistry and the future of the automobile, J. Phys. Chem. Lett. 1 (2010) 2204–2219.
[3] B.C. Steele, A. Heinzel, Materials for fuel-cell technologies, Nature 414 (2001) 345–352.
[4] A.S. Arico, S. Srinivasan, V. Antonucci, DMFCs: from fundamental aspects to technology development, Fuel Cells Weinh. (Weinh) 1 (2001) 133–161.
[5] Q. Li, T. Wang, D. Havas, H. Zhang, P. Xu, J. Han, J. Cho, G. Wu, High-performance direct methanol fuel cells with precious-metal-Free cathode, Adv. Sci. 3 (2016) 1600140.
[6] L. Osmieri, R. Escudero-Cid, M. Armandi, A.H.A. Monteverde Videla, J.L. García Fierro, P. Ocón, S. Specchia, Fe-N/C catalysts for oxygen reduction reaction supported on different carbonaceous materials. Performance in acidic and alkaline direct alcohol fuel cells, Appl. Catal. B-Environ. 205 (2017) 637–653.
[7] L. Osmieri, R. Escudero-Cid, A.H.A. Monteverde Videla, P. Ocón, S. Specchia, Performance of a Fe-N-C catalyst for the oxygen reduction reaction in direct methanol fuel cell: cathode formulation optimization and short-term durability, Appl. Catal. B-Environ. 201 (2017) 253–265.
[8] G. Wu, P. Zelenay, Nanostructured nonprecious metal catalysts for oxygen reduction reaction, Acc. Chem. Res. 46 (2013) 1878–1889.
[9] M.K. Debe, Electrocatalyst approaches and challenges for automotive fuel cells, Nature 486 (2012) 43–51.
[10] S.Q. Song, W.J. Zhou, W.Z. Li, G. Sun, Q. Xin, S. Kontou, P. Tsiakaras, Direct methanol fuel cells : methanol crossover and its influence on single DMFC performance, Ionics 10 (2004) 458–462.
[11] J. Suntivich, H.A. Gasteiger, N. Yabuuchi, H. Nakanishi, J.B. Goodenough, Y. Shao-Horn, Design principles for oxygen-reduction activity on perovskite oxide catalysts for fuel cells and metal-air batteries, Nat. Chem. 3 (2011) 546–550.
[12] K. Gong, F. Du, Z. Xia, M. Durstock, L. Dai, Nitrogen-doped carbon nanotube arrays with high electrocatalytic activity for oxygen reduction, Science 323 (2009) 760–764.
[13] M. Lefevre, E. Proietti, F. Jaouen, J.P. Dodelet, Iron-based catalysts with improved oxygen reduction activity in polymer electrolyte fuel cells, Science 324 (2009) 71–74.
[14] G. Wu, K.L. More, C.M. Johnston, P. Zelenay, High-performance electrocatalysts for oxygen reduction derived from polyaniline, iron, and cobalt, Science 332 (2011) 443–447.
[15] Y. Xu, B. Chen, J. Nie, G. Ma, Reactive template-induced core-shell FeCo@C microspheres as multifunctional electrocatalysts for rechargeable zinc-air batteries, Nanoscale 10 (2018) 17021–17029.
[16] M. Xiao, J. Zhu, L. Feng, C. Liu, W. Xing, Meso/macroporous nitrogen-doped carbon architectures with iron carbide encapsulated in graphitic layers as an efficient and robust catalyst for the oxygen reduction reaction in both acidic and alkaline solutions, Adv. Mater. 27 (2015) 2521–2527.
[17] D. Deng, L. Yu, X. Chen, G. Wang, L. Jin, X. Pan, J. Deng, G. Sun, X. Bao, Iron encapsulated within pod-like carbon nanotubes for oxygen reduction reaction, Angew. Chem. Int. Ed. 52 (2013) 371–375.
[18] E. Proietti, F. Jaouen, M. Lefevre, N. Larouche, J. Tian, J. Herranz, J.P. Dodelet, Iron-based cathode catalyst with enhanced power density in polymer electrolyte membrane fuel cells, Nat. Commun. 2 (2011) 416.
[19] Q. Lai, L. Zheng, Y. Liang, J. He, J. Zhao, J. Chen, Metal–Organic-Framework-Derived Fe-N/C electrocatalyst with five-coordinated Fe-Nx sites for advanced oxygen reduction in acid media, ACS Catal. 7 (2017) 1655–1663.
[20] M. Xiao, J. Zhu, L. Ma, Z. Jin, J. Ge, X. Deng, Y. Hou, Q. He, J. Li, Q. Jia, S. Mukerjee, R. Yang, Z. Jiang, D. Su, C. Liu, W. Xing, Microporous framework induced synthesis of single-atom dispersed Fe-N-C acidic ORR catalyst and its in situ reduced Fe-N4 active site identification revealed by X-ray absorption spectroscopy, ACS Catal. 8 (2018) 2824–2832.
[21] W.J. Jiang, L. Gu, L. Li, Y. Zhang, X. Zhang, L.J. Zhang, J.Q. Wang, J.S. Hu, Z. Wei, L.J. Wan, Understanding the high activity of Fe-N-C electrocatalysts in oxygen reduction: Fe/Fe3C nanoparticles boost the activity of Fe-N(x), J. Am. Chem. Soc. 138 (2016) 3570–3578.
[22] Y. Chen, S. Ji, Y. Wang, J. Dong, W. Chen, Z. Li, R. Shen, L. Zheng, Z. Zhuang, D. Wang, Y. Li, Isolated single Iron atoms anchored on N-Doped porous carbon as an efficient electrocatalyst for the oxygen reduction reaction, Angew. Chem. Int. Ed. 56 (2017) 6937–6941.
[23] H. Zhang, S. Hwang, M. Wang, Z. Feng, S. Karakalos, L. Luo, Z. Qiao, X. Xie, C. Wang, D. Su, Y. Shao, G. Wu, Single atomic Iron catalysts for oxygen reduction in acidic media: particle size control and thermal activation, J. Am. Chem. Soc. 139 (2017) 14143–14149.
[24] H.T. Chung, D.A. Cullen, D. Higgins, B.T. Sneed, E.F. Holby, K.L. More, P. Zelenay, Direct atomic-level insight into the active sites of a high-performance PGM-free ORR catalyst, Science 357 (2017) 479–484.
[25] Q. Liu, X. Liu, L. Zheng, J. Shui, The solid-phase synthesis of an Fe-N-C electrocatalyst for high-power proton-exchange membrane fuel cells, Angew. Chem. Int. Ed. 57 (2018) 1204–1208.
[26] L. Yang, D. Cheng, H. Xu, X. Zeng, X. Wan, J. Shui, Z. Xiang, D. Cao, Unveiling the high-activity origin of single-atom iron catalysts for oxygen reduction reaction, Proc. Natl. Acad. Sci. 115 (2018) 6626–6631.
[27] W. Gu, L. Hu, J. Li, E. Wang, Hybrid of g-C3N4 assisted metal-organic frameworks and their derived high-efficiency oxygen reduction electrocatalyst in the whole pH range, ACS appl, Mater. Interfaces 8 (2016) 35281–35288.
[28] S. Zhao, H. Yin, L. Du, L. He, K. Zhao, L. Chang, G. Yin, H. Zhao, S. Liu, Z. Tang, Carbonized nanoscale metal-organic frameworks as high performance electrocatalyst for oxygen reduction reaction, ACS Nano 8 (2014) 12660–12668.
[29] D. Guo, S. Han, J. Wang, Y. Zhu, MIL-100-Fe derived N-doped Fe/Fe 3 C@C electrocatalysts for efficient oxygen reduction reaction, Appl. Surf. Sci. 434 (2018) 1266–1273.
[30] J.S. Li, S.L. Li, Y.J. Tang, M. Han, Z.H. Dai, J.C. Bao, Y.Q. Lan, Nitrogen-doped Fe/Fe3C@graphitic layer/carbon nanotube hybrids derived from MOFs: efficient bifunctional electrocatalysts for ORR and OER, Chem. Commun. (Camb.) 51 (2015) 2710–2713.
[31] D. Zhao, J.-L. Shui, C. Chen, X. Chen, B.M. Reprogle, D. Wang, D.-J. Liu, Iron imidazolate framework as precursor for electrocatalysts in polymer electrolyte membrane fuel cells, Chem. Sci. 3 (2012) 3200.
[32] B.Y. Guan, L. Yu, X.W. Lou, A dual-metal–organic-framework derived electrocatalyst for oxygen reduction, Energy Environ, Sci. 9 (2016) 3092–3096.
[33] Y. Ye, F. Cai, H. Li, H. Wu, G. Wang, Y. Li, S. Miao, S. Xie, R. Si, J. Wang, X. Bao, Surface functionalization of ZIF-8 with ammonium ferric citrate toward high exposure of Fe-N active sites for efficient oxygen and carbon dioxide electroreduction, Nano Energy 38 (2017) 281–289.
[34] C. Mao, A. Kong, Y. Wang, X. Bu, P. Feng, MIL-100 derived nitrogen-embodied carbon shells embedded with iron nanoparticles, Nanoscale 7 (2015) 10817–10822.
[35] J. Wang, G. Han, L. Wang, L. Du, G. Chen, Y. Gao, Y. Ma, C. Du, X. Cheng, P. Zuo, G. Yin, ZIF-8 with ferrocene encapsulated: a promising precursor to single-atom Fe embedded nitrogen-doped carbon as highly efficient catalyst for oxygen electroreduction, Small 14 (2018) 1704282.
[36] S.H. Ahn, X. Yu, A. Manthiram, "Wiring" Fe-Nx -Embedded Porous Carbon Framework onto 1D Nanotubes for Efficient Oxygen Reduction Reaction in Alkaline and Acidic Media, Adv. Mater. 29 (2017) 1606534.
[37] Q. Niu, J. Guo, Y. Tang, X. Guo, J. Nie, G. Ma, Sandwich-type bimetal-organic Frameworks/Graphene oxide derived porous nanosheets doped Fe/Co-N active sites for oxygen reduction reaction, Electrochim. Acta 255 (2017) 72–82.
[38] D.-Y. Hong, Y.K. Hwang, C. Serre, G. Férey, J.-S. Chang, Porous chromium terephthalate MIL-101 with coordinatively unsaturated sites: surface functionalization, encapsulation, sorption and catalysis, Adv. Funct. Mater. 19 (2009) 1537–1552.
[39] L. Yang, Y. Zeng, X. Tang, D. Xu, D. Fang, H. Huang, Z. Shao, B. Yi, Self-sacrificial template synthesis of a nitrogen-doped microstructured carbon tube as electrocatalyst for oxygen reduction, ChemElectroChem 5 (2018) 3731–3740.
[40] P. Zhao, X. Hua, W. Xu, W. Luo, S. Chen, G. Cheng, Metal–organic framework-derived hybrid of Fe3C nanorod-encapsulated, N-doped CNTs on porous carbon sheets for highly efficient oxygen reduction and water oxidation, Catal. Sci. Technol. 6 (2016) 6365–6371.
[41] J. Cravillon, S. Münzer, S.-J. Lohmeier, A. Feldhoff, K. Huber, M. Wiebcke, Rapid room-temperature synthesis and characterization of nanocrystals of a prototypical zeolitic imidazolate framework, Chem. Mater. 21 (2009) 1410–1412.
[42] T. Yamada, K. Shiraishi, H. Kitagawa, N. Kimizuka, Applicability of MIL-101(Fe) as a cathode of lithium ion batteries, Chem. Commun. (Camb.) 53 (2017) 8215–8218.
[43] A. Kong, X. Zhu, Z. Han, Y. Yu, Y. Zhang, B. Dong, Y. Shan, Ordered hierarchically Micro- and mesoporous Fe–Nx-Embedded graphitic architectures as efficient electrocatalysts for oxygen reduction reaction, ACS Catal. 4 (2014) 1793–1800.
[44] G.A. Ferrero, K. Preuss, A. Marinovic, A.B. Jorge, N. Mansor, D.J.L. Brett, A.B. Fuertes, M. Sevilla, M.-M. Titirici, Fe–N-Doped carbon capsules with outstanding electrochemical performance and stability for the oxygen reduction reaction in both acid and alkaline conditions, ACS Nano 10 (2016) 5922–5932.
[45] Z. Wen, S. Ci, F. Zhang, X. Feng, S. Cui, S. Mao, S. Luo, Z. He, J. Chen, Nitrogen-enriched core-shell structured Fe/Fe(3)C-C nanorods as advanced electrocatalysts for oxygen reduction reaction, Adv. Mater. 24 (2012) 1399–1404.
[46] H.R. Byon, J. Suntivich, Y. Shao-Horn, Graphene-based non-noble-Metal catalysts for oxygen reduction reaction in acid, Chem. Mater. 23 (2011) 3421–3428.
[47] Z. Zhang, J. Sun, F. Wang, L. Dai, Efficient oxygen reduction reaction (ORR) catalysts based on single Iron atoms dispersed on a hierarchically structured porous carbon framework, Angew. Chem. Int. Ed. 57 (2018) 9038–9043.
[48] U.I. Kramm, M. Lefevre, N. Larouche, D. Schmeisser, J.P. Dodelet, Correlations between mass activity and physicochemical properties of Fe/N/C catalysts for the ORR in PEM fuel cell via 57Fe Mossbauer spectroscopy and other techniques, J. Am. Chem. Soc. 136 (2014) 978–985.
[49] A. Zitolo, V. Goellner, V. Armel, M.T. Sougrati, T. Mineva, L. Stievano, E. Fonda, F. Jaouen, Identification of catalytic sites for oxygen reduction in iron- and nitrogen-doped graphene materials, Nat. Mater. 14 (2015) 937–942.
[50] U.I. Kramm, J. Herranz, N. Larouche, T.M. Arruda, M. Lefevre, F. Jaouen, P. Bogdanoff, S. Fiechter, I. Abs-Wurmbach, S. Mukerjee, J.P. Dodelet, Structure of the catalytic sites in Fe/N/C-catalysts for O2-reduction in PEM fuel cells, Phys. Chem. Chem. Phys. 14 (2012) 11673–11688.
[51] X.W. Liu, S. Zhao, Y. Meng, Q. Peng, A.K. Dearden, C.F. Huo, Y. Yang, Y.W. Li, X.D. Wen, Mossbauer spectroscopy of Iron carbides: from prediction to experimental confirmation, Sci. Rep. 6 (2016) 26184.
[52] H. Fei, J. Dong, Y. Feng, C.S. Allen, C. Wan, B. Volosskiy, M. Li, Z. Zhao, Y. Wang, H. Sun, P. An, W. Chen, Z. Guo, C. Lee, D. Chen, I. Shakir, M. Liu, T. Hu, Y. Li, A.I. Kirkland, X. Duan, Y. Huang, General synthesis and definitive structural identification of MN4C4 single-atom catalysts with tunable electrocatalytic activities, Nat. Catal. 1 (2018) 63–72.
[53] L. Zheng, Y. Dong, B. Chi, Z. Cui, Y. Deng, X. Shi, L. Du, S. Liao, UIO-66-NH2 -Derived mesoporous carbon catalyst Co-doped with Fe/N/S as highly efficient cathode catalyst for PEMFCs, Small 15 (2019) e1803520.
[54] Y. Cao, Y. Meng, S. Huang, S. He, X. Li, S. Tong, M. Wu, Nitrogen-, oxygen- and sulfur-doped carbon-encapsulated Ni3S2 and NiS core–shell architectures: bifunctional electrocatalysts for hydrogen evolution and oxygen reduction reactions, ACS Sustainable Chem. Eng. 6 (2018) 15582–15590.
[55] S.C. Huang, Y.Y. Meng, S.M. He, A. Goswami, Q.L. Wu, J.H. Li, S.F. Tong, T. Asefa, M.M. Wu, N-, O-, and S-Tridoped Carbon-Encapsulated Co9S8 Nanomaterials: Efficient Bifunctional Electrocatalysts for Overall Water Splitting, Adv. Funct.

Mater. 27 (2017) 1606585.
[56] S. Huang, Y. Meng, Y. Cao, S. He, X. Li, S. Tong, M. Wu, N-, O- and P-doped hollow carbons: Metal-free bifunctional electrocatalysts for hydrogen evolution and oxygen reduction reactions, Appl. Catal. B-Environ. 248 (2019) 239–248.
[57] K. Artyushkova, I. Matanovic, B. Halevi, P. Atanassov, Oxygen binding to active sites of Fe–N–C ORR electrocatalysts observed by ambient-pressure XPS, J. Phys. Chem. C 121 (2017) 2836–2843.
[58] M. Ferrandon, A.J. Kropf, D.J. Myers, K. Artyushkova, U. Kramm, P. Bogdanoff, G. Wu, C.M. Johnston, P. Zelenay, Multitechnique characterization of a polyaniline–Iron–Carbon oxygen reduction catalyst, J. Phys. Chem. C 116 (2012) 16001–16013.
[59] W. Xia, J. Zhu, W. Guo, L. An, D. Xia, R. Zou, Well-defined carbon polyhedrons prepared from nano metal–organic frameworks for oxygen reduction, J. Mater. Chem. A Mater. Energy Sustain. 2 (2014) 11606.
[60] E. Frackowiak, F. Beguin, Carbon materials for the electrochemical storage of energy in capacitors, Carbon 39 (2001) 937–950.
[61] Q. Wang, Z.Y. Zhou, Y.J. Lai, Y. You, J.G. Liu, X.L. Wu, E. Terefe, C. Chen, L. Song, M. Rauf, N. Tian, S.G. Sun, Phenylenediamine-based FeN(x)/C catalyst with high activity for oxygen reduction in acid medium and its active-site probing, J. Am. Chem. Soc. 136 (2014) 10882–10885.